EASR

Engineering and Applied Science Research

https://www.tci-thaijo.org/index.php/easr/index

Published by the Faculty of Engineering, Khon Kaen University, Thailand

Corrosion behavior of CA6NM in simulated geothermal brine highlighted by Electrochemical Impedance Spectroscopy (EIS)

Arini Nikitasari*[1)], Efendi Mabruri[1)] and Rini Riastuti[2)]

[1)]Research Center for Metallurgy and Materials, Indonesian Institute of Sciences, South Tangerang, 15313, Indonesia
[2)]Department of Metallurgy and Materials, Faculty of Engineering, University of Indonesia, Depok, 16424, Indonesia

Received 2 June 2020
Revised 6 October 2020
Accepted 29 October 2020

Abstract

Martensitic stainless steel CA6NM has the potential to be utilized as a turbine blade material for geothermal power plants because of its superior mechanical properties. However, the turbine blade material for geothermal power plants must have not only superior mechanical properties but also excellent corrosion resistance. Therefore, in this study, CA6NM was modified by varying its molybdenum (Mo) and nitrogen (N) contents to improve its corrosion resistance in the geothermal environment. The Mo and N contents of CA6NM were modified as follows: CA6NM1 with 1% Mo, CA6NM2 with 2% Mo, and CA6NM3 with 2% Mo and 0.1% N. Two temperature parameters, i.e., room temperature and 60°C, and two CO_2 gas parameters, i.e., presence and absence of CO_2 gas, were utilized in this study. To understand the corrosion behavior of modified CA6NM in geothermal brine, the electrochemical impedance spectroscopy (EIS) test was performed in simulated geothermal brine. The results of the EIS test showed that both Mo and N can increase the corrosion resistance of CA6NM in simulated geothermal brine at 60°C.

Keywords: EIS, CA6NM, Geothermal, Turbine blade, Molybdenum

1. Introduction

The geothermal environment has many aggressive substances that induce corrosion. One problem that needs to be evaluated in geothermal power plants is the corrosion of the turbine blade [1, 2]. Currently, steam scrubbing and chloride subtraction with sodium hydroxide are used to mitigate the corrosion of the turbine blade. However, these techniques can increase the operating costs and reduce the efficiency of geothermal power plants. Thus, the use of corrosion-resistant materials, such as a geothermal turbine blade, can be a better solution [3].

On the basis of the material selection guidelines, stainless steel is mainly recommended for use in the geothermal turbine blade. Stainless steel is resistant to corrosion because of its passive film [4]. Nevertheless, the passive film of stainless steel can be destroyed in high-chloride environments, such as geothermal brine. Thereby, stainless steel needs to be modified to increase the service life of the geothermal turbine blade. CA6NM is martensitic stainless steel that exhibits better corrosion resistance than standard stainless steel because of alloy modification [5, 6], which is performed by the addition of molybdenum (Mo).

Mo and nitrogen (N) can improve the corrosion resistance of stainless steel [4]. The addition of the optimum ranges of Mo and N to the alloy composition will improve the corrosion properties of martensitic stainless steel. When Mo and N in the alloy composition exceed the optimum ranges, the properties of the alloy deteriorate because of the absence of the passive film on the surface, formation of δ-ferrite, decrease in toughness, and excess precipitation [7]. Hence, the optimum ranges of Mo and N in the alloy composition of martensitic stainless steel CA6NM need to be determined.

At present, the role of alloyed Mo and N in increasing corrosion resistance has been widely investigated. However, data on CA6NM in the geothermal environment are still lacking. This study aims to investigate the influence of Mo and N contents on the corrosion behavior of CA6NM in simulated geothermal brine at 60°C using electrochemical impedance spectroscopy (EIS). EIS is a nondestructive technique that can provide time-dependent quantitative information about the electrode processes, complex interfaces, and characteristics of materials, such as high-resistivity materials (e.g., paint and oxide coating) [8, 9]. EIS is used in this experiment because it is a powerful technique that can highlight the effect of alloying elements on the corrosion resistance of the metallic surface [10].

2. Materials and methods

Specimens were prepared by casting martensitic stainless steel CA6NM with three variations of Mo and N contents. The chemical compositions of the CA6NM specimens used in this experiment are presented in Table 1. All specimens were austenitized at 1,323 K (or 1,050°C) for 3 h and quenched in oil. Then, the austenitized specimens were tempered at 943 K (or 670°C) for 3 h, followed by air cooling to room temperature. The specimens with a surface area of 1.21 cm^2 were cut using a cutting machine, connected with copper

*Corresponding author. Tel.: +628 5286 2443
Email address: arininikitasari89@gmail.com
doi: 10.14456/easr.2021.38

wire for electrical contact, and mounted with resin to cover the unexposed area. The specimens were polished using 120-1,200 grit SiC paper and washed with distilled water.

Table 1 Chemical compositions of CA6NM specimens

Specimens	C [%]	Mn [%]	Si [%]	P [%]	S [%]	Cr [%]	Ni [%]	Mo [%]	N [%]	Fe [%]
CA6NM1	0.04	0.40	0.35	0.018	0.008	12.83	4.17	1.02	–	Bal
CA6NM2	0.04	0.43	0.55	0.017	0.009	13.02	4.08	1.96	–	Bal
CA6NM3	0.04	0.35	0.35	0.019	0.009	13.07	4.09	2.14	0.11	Bal

Table 2 Chemical compositions of simulated geothermal brine

Chemical	Concentration [g/L]
NaCl	224.6
$NaSO_4 \cdot 10H_2O$	12.1
$MgCl \cdot 6H_2O$	10.6
$CaCl_2 \cdot 2H_2O$	6.5
KCl	0.4
KOH	0.3
$NaHCO_3$	0.05

The electrochemical measurement of the specimens was conducted using the Gamry G750 corrosion measurement system in simulated geothermal brine. The chemical composition of the simulated geothermal brine is listed in Table 2. A hot plate and a thermometer are used to adjust and control the temperature at 60°C. The presence or absence of CO_2 gas in simulated geothermal brine was a parameter that varied in this study. The electrochemical measurement used three electrodes, i.e., the specimens as the working electrode, a graphite rod as the counter electrode, and a saturated calomel electrode as the reference electrode. The specimens were immersed in 500 mL of simulated geothermal brine and left to corrode freely for 1 h in the solution until the steady-state condition was reached. Under the steady-state condition, the open-circuit potential (E_{oc}) was recorded, and the electrochemical measurement started from the initial value of E_{oc}.

The EIS test was conducted to investigate the charge transfer resistance (R_{ct}) and constant phase element (CPE; Y_0) values. The EIS test measures the impedance of the specimens with the sinusoidal voltage signal of 10 mV and the frequency range of 100 kHz to 10 MHz using the Gamry G750 corrosion measurement system. After the EIS test, the exposed surface of all samples was observed using a scanning electron microscope (JEOL Model JSM-5400).

3. Results

Figures 1(a)-(d) show the Nyquist plots of the CA6NM specimens with different Mo and N contents immersed in simulated geothermal brine.

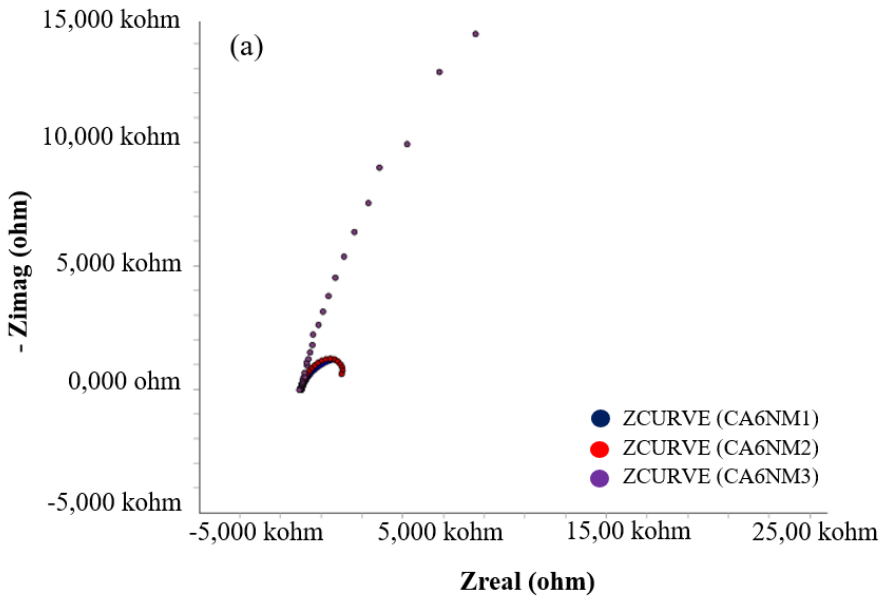

Figure 1 Nyquist plots of the CA6NM specimens in simulated geothermal brine at (a) room temperature without CO_2 gas, (b) room temperature with CO_2 gas, (c) 60°C without CO_2 gas, and (d) 60°C with CO_2 gas

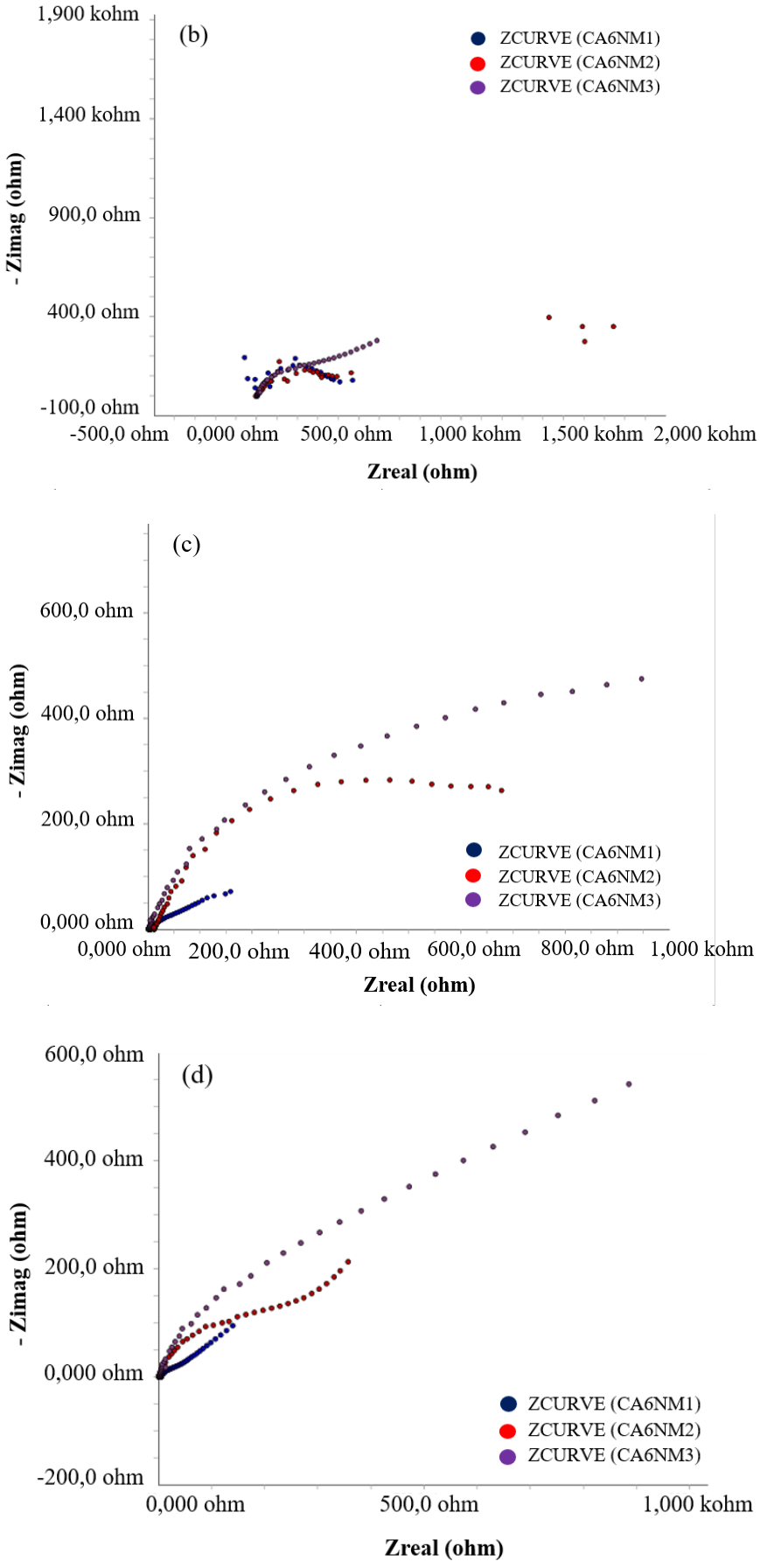

Figure 1 (continued) Nyquist plots of the CA6NM specimens in simulated geothermal brine at (a) room temperature without CO_2 gas, (b) room temperature with CO_2 gas, (c) 60°C without CO_2 gas, and (d) 60°C with CO_2 gas

The Bode plots of the CA6NM specimens in simulated geothermal brine are shown in Figure 2. The Bode and Nyquist plots are diagrams generated from the results of the EIS test.

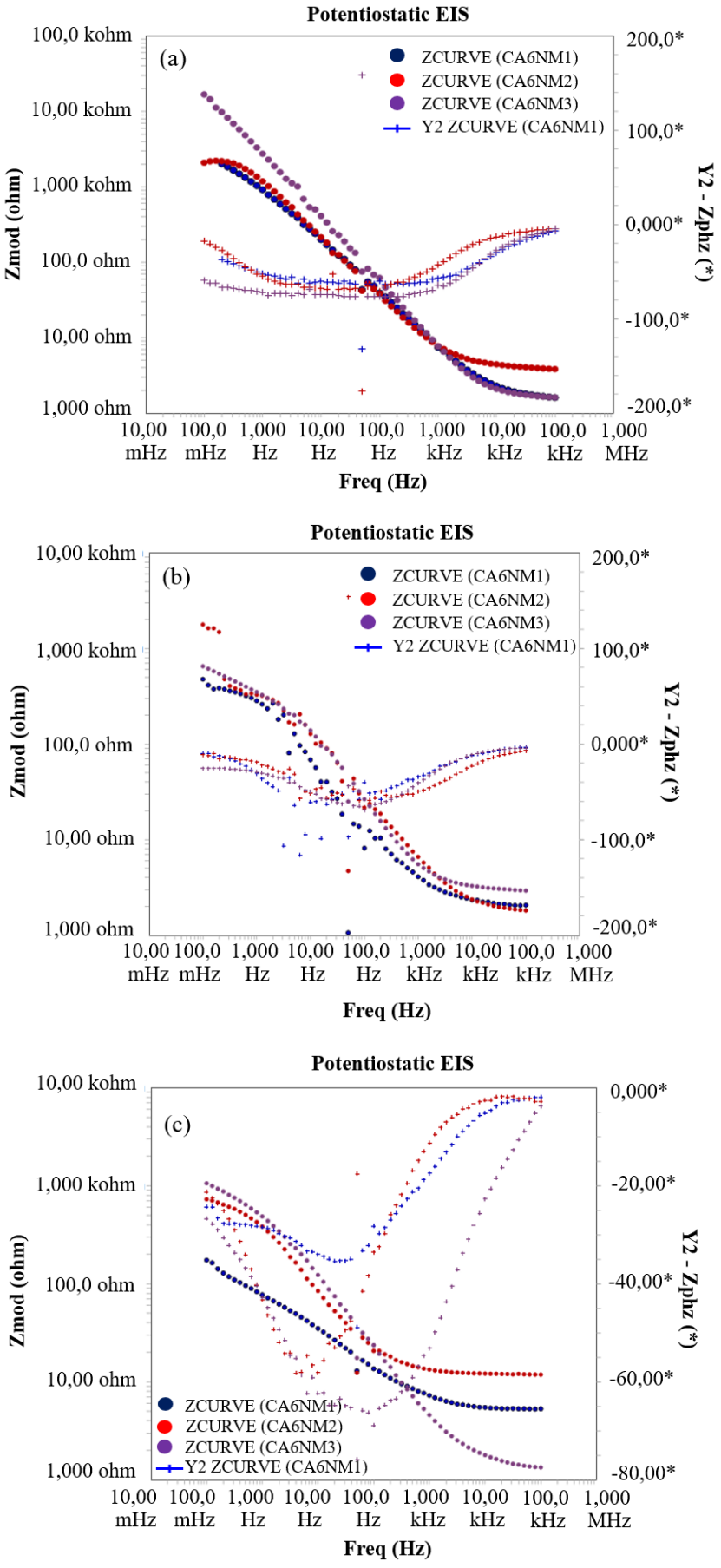

Figure 2 Bode plot of the CA6NM specimens in simulated geothermal brine at (a) room temperature without CO_2 gas, (b) room temperature with CO_2 gas, (c) 60°C without CO_2 gas, and (d) 60°C with CO_2 gas

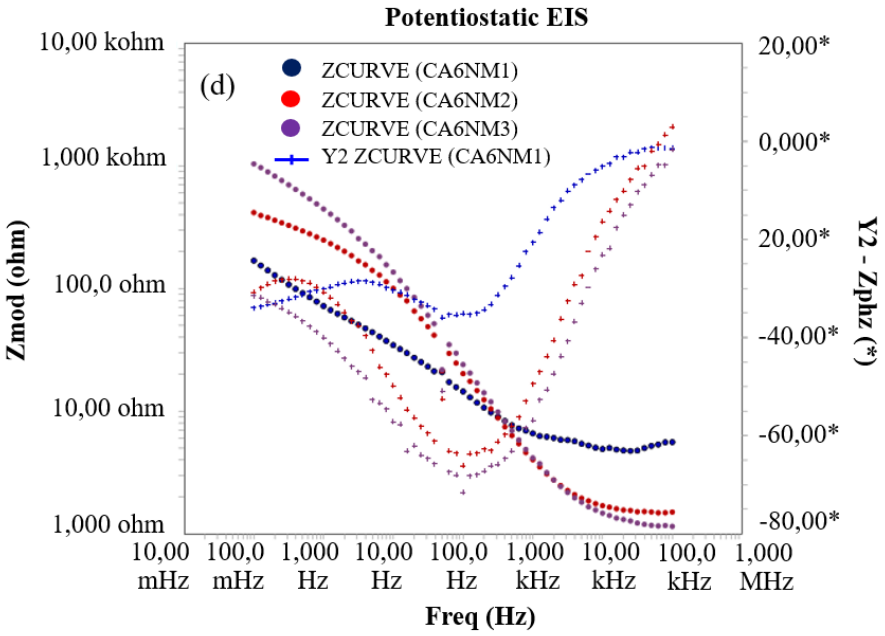

Figure 2 (continued) Bode plot of the CA6NM specimens in simulated geothermal brine at (a) room temperature without CO_2 gas, (b) room temperature with CO_2 gas, (c) 60°C without CO_2 gas, and (d) 60°C with CO_2 gas

The scanning electron microscopy (SEM) images of the CA6NM specimens in simulated geothermal brine at room temperature are shown in Figures 3 and 4. Meanwhile, the SEM images of the CA6NM specimens in simulated geothermal brine at 60°C are shown in Figures 5 and 6. Figures 3-6 also show the SEM images of the CA6NM specimens after the EIS test.

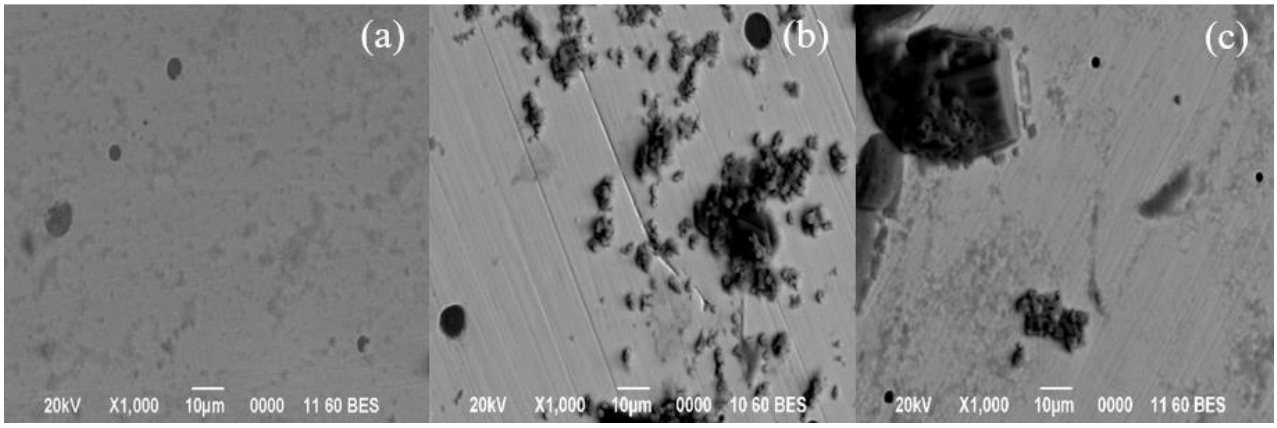

Figure 3 SEM images of (a) CA6NM1, (b) CA6NM2, and (c) CA6NM3 in simulated geothermal brine at room temperature without CO_2 gas

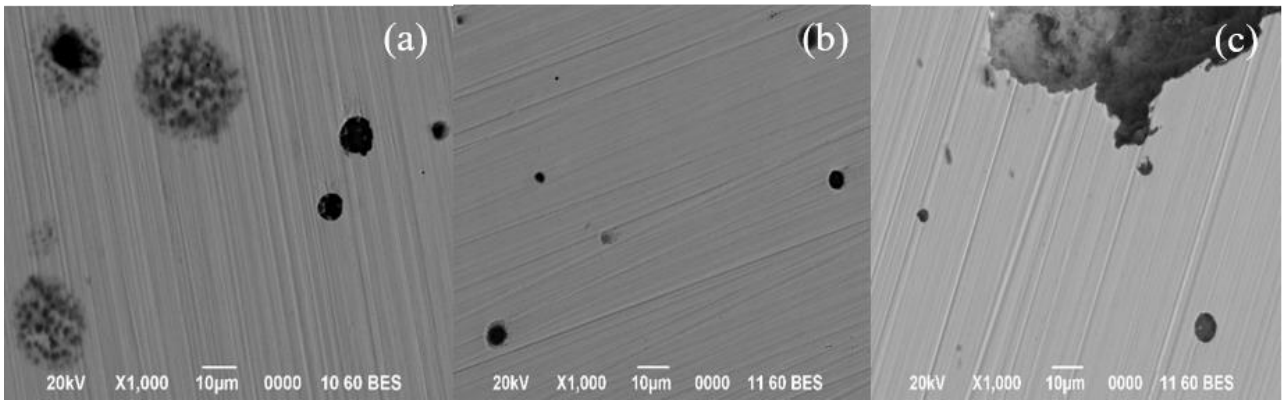

Figure 4 SEM images of (a) CA6NM1, (b) CA6NM2, and (c) CA6NM3 in simulated geothermal brine at room temperature with CO_2 gas

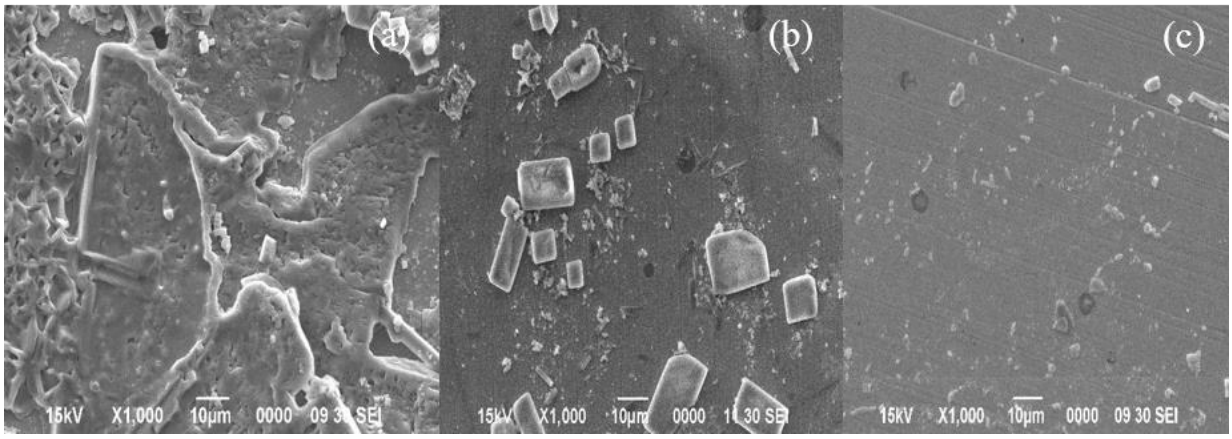

Figure 5 SEM images of (a) CA6NM1, (b) CA6NM2, and (c) CA6NM3 in simulated geothermal brine at 60°C without CO_2 gas

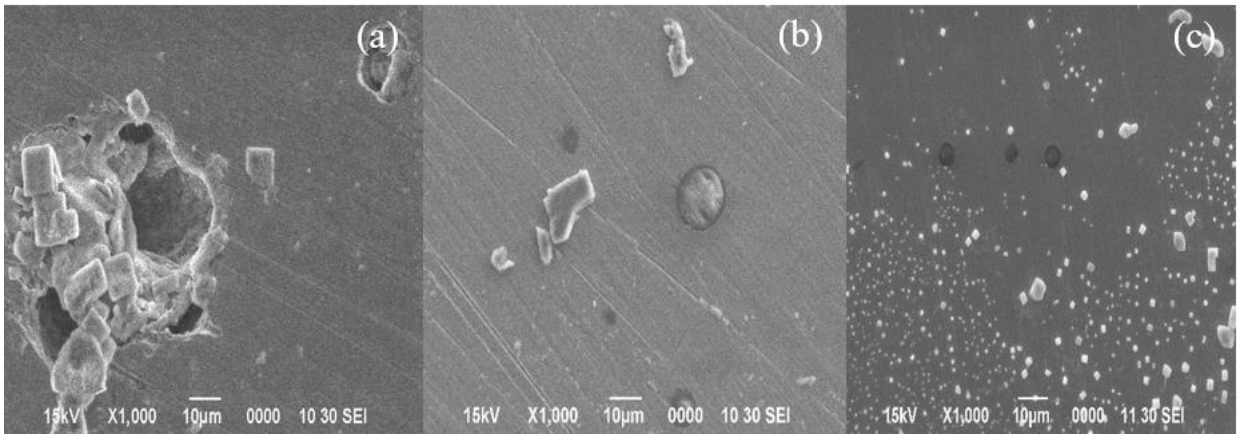

Figure 6 SEM images of (a) CA6NM1, (b) CA6NM2, and (c) CA6NM3 in simulated geothermal brine at 60°C with CO_2 gas

In conjunction with SEM, energy-dispersive X-ray spectroscopy (EDS) is employed to conduct chemical microanalysis. Table 3 lists the chromium (Cr) contents of the CA6NM specimens in simulated geothermal brine at 60°C determined by EDS.

Table 3 Chromium contents of the CA6NM specimens in simulated geothermal brine at 60°C

Specimens	Cr (wt%)
CA6NM1 without CO_2 gas	3.6
CA6NM2 without CO_2 gas	10.7
CA6NM3 without CO_2 gas	13.6
CA6NM1 with CO_2 gas	12.4
CA6NM2 with CO_2 gas	13.5
CA6NM3 with CO_2 gas	13.5

4. Discussion

4.1 Role of Mo and N contents

The EIS Nyquist plots of the CA6NM specimens in simulated geothermal brine are shown in Figure 1. As shown in Figure 1, the order of the slope and size changes of the impedance arcs of the CA6NM specimens is CA6NM3 > CA6NM2 > CA6NM1. The semicircle diameter of the Nyquist plot increases with the increase in Mo and N contents. Moreover, the semicircle diameter of the Nyquist plot of the CA6NM3 specimen did not increase. The impedance of CA6NM3 continues to increase with the increase in all of the experimental parameters. This finding indicates that the number of electrons/ions in the CA6NM3 interface is limited because of the stable passive layer on the CA6NM3 surface [11-12].

The Bode plots illustrated in Figures 2(a)-(d) show the impedance and phase angle values of the CA6NM specimens at each frequency. Bode plot analysis can be divided into two parts on the basis of its frequency, namely, high frequency with a value of $f >$ 100 Hz and low frequency with a value of $f <$ 10 Hz. At high frequency, the Bode plot of the phase angle shows whether the passive layer formed on the surface of the material is protective or not. As shown in Figure 2, all CA6NM specimens have a phase angle value that is close to 0 at high frequency. These results indicate that the surfaces of the CA6NM specimens are resistant to the aggressive substances in the geothermal environment or that the passive layer or oxide film formed on the surface of the surfaces of the CA6NM specimens is protective. The impedance value of CA6NM at low frequency indicates the strength of the formed passive layer, where the higher the impedance value at low frequency is, the better the corrosion resistance of the formed passive layer. As shown in Figure 2, the CA6NM3 specimen has the highest impedance value at low frequency in all of the experimental parameters and conditions.

Both Nyquist and Bode plots indicate that the Mo and N contents have a positive role in improving the corrosion resistance of CA6NM in simulated geothermal brine. This result is consistent with that of Monnot et al., where the addition of Mo improves the corrosion resistance of martensitic stainless steel [10]. Similar to that generated from the results of the present research, the Nyquist plot generated from the results of the EIS test conducted by Monnot et al. showed that the impedance behavior is characterized by depressed capacitive loops with a clear increasing modulus trend with the Mo content, confirming the beneficial effect of Mo. Mo has two beneficial effects on the corrosion resistance of martensitic stainless steel, i.e., improving the strength of the passive film and inducing an increase in the retained austenite fraction.

Moreover, the results of Loable et al. indicate that the synergy between Mo and N has a positive effect on the pitting corrosion of austenitic stainless steel [4]. Loable et al. analyzed the capacitance parameter by conducting the EIS test using the Hsu and Manfield formula. The capacitance effect (C_{eff}) is inversely proportional to the thickness of the passive film. Loable et al. determined that 18Cr-12Ni-3Mo-0.1N had a lower C_{eff} than 18Cr-12Ni-3Mo, indicating that 18Cr-12Ni-3Mo-0.1N had a thicker passive film than 18Cr-12Ni-3Mo. The thicker the passive film is, the better the corrosion resistance. Similar to those of Loable et al., the results of the present research confirm the synergetic positive effect of the addition of both Mo and N on the corrosion resistance of martensitic stainless steel in simulated geothermal brine.

4.2 Influence of temperature and CO2 gas on corrosion behavior

The characterization of electrochemical systems by EIS requires the interpretation of data and involves the use of the electrode equivalent circuit (EEC) [13]. The EEC is an electrical circuit model that is suitable for the electrochemical system of the specimens. The EEC for CA6NM in simulated geothermal brine is shown in Figure 7. Meanwhile, the EEC for CA6NM in simulated geothermal brine at 60°C with CO_2 gas is shown in Figure 8. The EEC illustrated in Figure 7 includes solution resistance (R_S) in series with a parallel connection of CPE and charge transfer resistance (R_{ct}). Element R_S corresponds to simulated geothermal brine, whereas element R_{ct} corresponds to charge transfer resistance in the phase interface and is inversely proportional to the corrosion rate and surface area undergoing corrosion. The CPE was introduced to characterize "capacitance dispersion" related to the capacity of the surface area of a material with complex surface roughness, inhomogeneous reaction rate, and nonuniform current distribution. The CPE has a fixed phase shift angle, and its impedance is expressed as $ZCPE = 1/Y_0(j\omega)n$, where Y_0 and a are the parameters related to the phase shift angle. The value of the parameter a denotes the corrosion process on the surface of the material, and the smaller the value of this parameter is, the more heterogeneous the process. The value of the parameter a also denotes adjustable inductance, where 1 corresponds to a capacitor and −1 corresponds to a resistor [13].

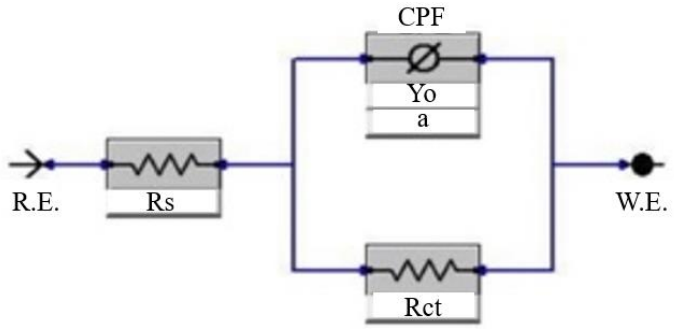

Figure 7 EEC of CA6NM in simulated geothermal brine

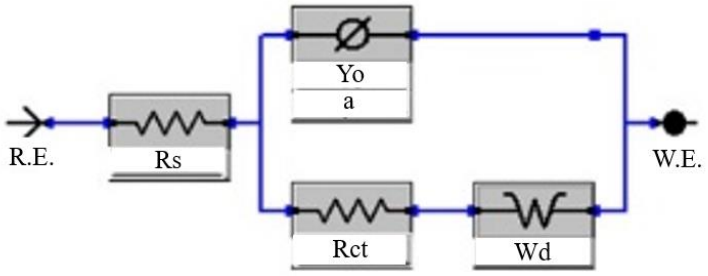

Figure 8 EEC of CA6NM in simulated geothermal brine at 60°C with CO_2 gas

The EEC of CA6NM in simulated geothermal brine at 60°C with CO_2 gas is different from that of the other specimens. The difference lies in the Warburg impedance (W_d) element in series with the charge transfer resistance (R_{ct}). The Warburg impedance shown in Figure 8 corresponds to the diffusion-controlled reaction at low frequency. The phase shift of Warburg impedance is equal to ϕ = -45°, and in the Nyquist plot, the Warburg impedance is represented by a straight line at 45° angle at low frequency, as shown in Figure 1(d) [8]. The appearance of the Warburg impedance in simulated geothermal brine at 60°C with CO_2 gas indicates the occurrence of CO_2 gas diffusion on the surface of CA6NM. CO_2 gas diffuses on the surface of the material and forms $FeCO_3$, which can protect the material from corrosion. The value of the Warburg impedance is 8.36E-03, 4.35E-3, and 1.68E-3 Ωcm^2 for CA6NM1, CA6NM2, and CA6NM3, respectively. The Warburg impedance decreases with the increase in Mo content. This result shows that CO_2 gas diffusion decreases because of the thick layer of molybdenum oxide on the surface of CA6NM. In terms of the other experimental parameters, the Warburg impedance does not appear because the diffusion process does not occur. The diffusion does not occur because CO_2 gas is not added to the simulated geothermal brine. However, even with the addition of CO_2 gas at room temperature, diffusion does not occur because CO_2 is unable to diffuse and form $FeCO_3$ at room temperature.

The EEC is fitted to the Nyquist plot, and the values of the electrochemical parameters, such as charge transfer resistance (R_{ct}) and CPE (Y_0), are obtained and used to analyze the corrosion resistance of CA6NM in the geothermal environment. Figure 9 shows the charge transfer resistance (R_{ct}) value and Figure 10 shows the CPE (Y_0) value of CA6NM in simulated geothermal brine. As shown in Figure 9, CA6NM3 has a higher charge transfer resistance (R_{ct}) value than CA6NM1 and CA6NM2. The charge transfer resistance (R_{ct}) value increases with the increase in Mo and N contents [14-16]. The increase in the charge transfer resistance (R_{ct}) value indicates charge transfer from the solution to the surface of CA6NM. However, charge transfer is inhibited by a thick passive film. CA6NM3 in simulated geothermal brine at room temperature without CO_2 gas has the highest charge transfer resistance (R_{ct}) value of 31.490 Ωcm^2.

The CPE (Y_0) value corresponds to the thickness of the passive film on the surface of the material. A low CPE (Y_0) value indicates a thick passive film. As shown in Figure 10, CA6NM3 has the lowest CPE (Y_0) value. This result proves that the increase in Mo and N contents of CA6NM specimens causes the passive film on the material surface to become thicker. Moreover, the increase in Mo and N contents leads to the formation of a thicker molybdenum oxide film on top of the chromium oxide (CrO_2) film. The thicker the molybdenum oxide film is, the stronger the passive film and the better the corrosion resistance of CA6NM. Figure 10(a) shows that the CPE (Y_0) values of CA6NM specimens without CO_2 gas in simulated geothermal brine are nearly the same. By contrast, Figure 10(b) shows that the CPE (Y_0) values of CA6NM specimens with CO_2 gas in simulated geothermal brine considerably vary. These results indicate that thick passive films are formed in the test solution at room temperature without CO_2 gas and at 60°C temperature with CO_2 gas.

The results of the EIS test show that CA6NM in geothermal solution at room temperature without CO_2 gas has better corrosion resistance than CA6NM in geothermal solution at room temperature with CO_2 gas because of its thicker passive film. This result is consistent with that of a previous study of the pitting corrosion resistance of CA6NM as geothermal turbine blade material in simulated geothermal brine [17]. The previous research focused on localized or pitting corrosion analyzed using cyclic polarization, whereas the present research focused on general corrosion analyzed using EIS under two temperature conditions.

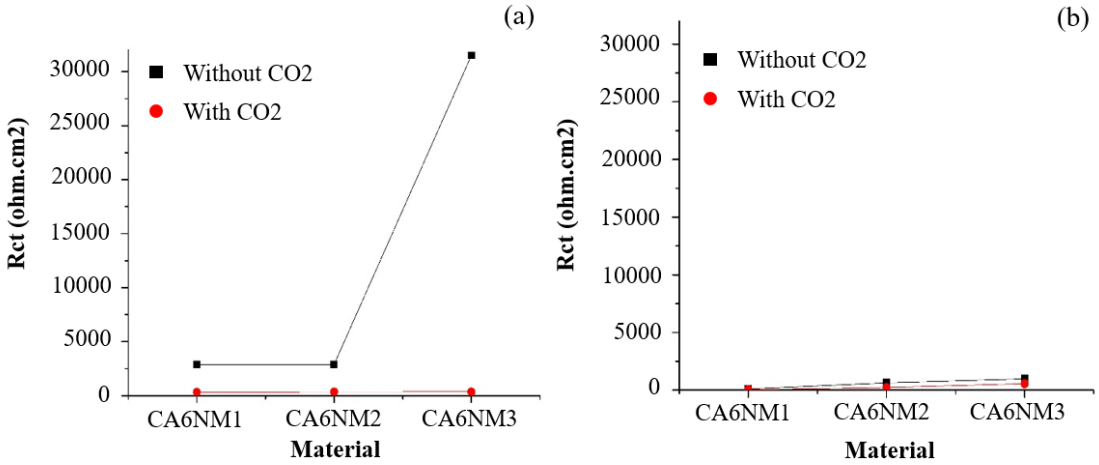

Figure 9 Charge transfer resistance (R_{ct}) values of CA6NM in simulated geothermal brine at (a) room temperature and (b) 60°C

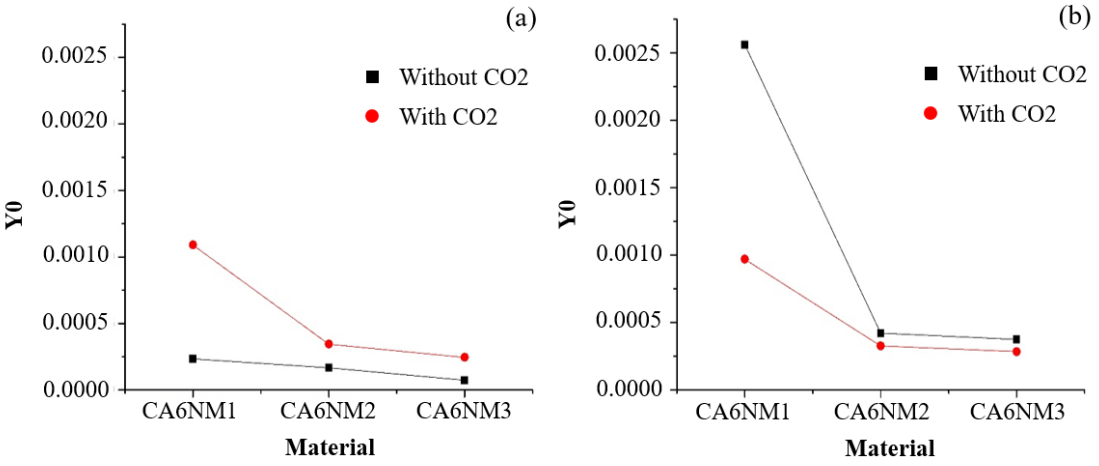

Figure 10 CPE (Y_0) values of CA6NM in simulated geothermal brine at (a) room temperature and (b) 60°C

4.3 SEM and EDS analyses

The effect of the addition of Mo and N on the pit growth behavior of CA6NM in simulated geothermal brine was investigated by SEM. As shown in Figures 3-6, spherical pitting corrosion formed on the surface of CA6NM with an average diameter size of <10 μm. The diameter size of pitting corrosion decreases with the increase in Mo and N contents.

In the case of CA6NM in simulated geothermal brine at room temperature, as shown in Figures 3 and 4, nearly no low-solubility salt film is formed on the inner surface. Thus, pit growth is considered to be stable at room temperature. By contrast, at 60°C, as shown in Figures 5 and 6, thick salt films are formed inside the pits or covered the pit mouths [18]. In particular, as shown in Figure 6(b), pit

growth on the inner layer results in the stunting of the pit. This result indicates that CA6NM2 in simulated geothermal brine at 60°C with CO_2 gas is resistant to localized corrosion because of the pace of repassivation [17].

To further prove the effect of Mo and N on the passive layer (CrO_2) of CA6NM, an EDS test of the surface of the material is conducted. Table 3 shows the Cr levels of CA6NM that had undergone EIS testing at 60°C on the basis of the EDS results. Table 3 also shows that the Cr levels increase with the addition of Mo and N. These results prove that Mo and N play an important role in inhibiting the dissolution of the passive layer, leading to a decrease in the Cr levels in the CA6NM1 specimen after the EIS test.

In addition to stabilizing the passive layer, Mo refines the grain size, which in turn improves the corrosion resistance of CA6NM [19]. Mo also reduces the formation of a Cr-depleted zone around the carbide area that initiates pitting corrosion because Mo can partially substitute Cr in metal carbide [20]. Finally, the results of the EDS test listed in Table 3 show that the Cr content increases with the increase in Mo content of CA6NM.

5. Conclusions

In conclusion, this study shows that Mo and N have a beneficial effect on the corrosion resistance of CA6NM in simulated geothermal brine. The results of the EIS test show that CA6NM3, which contains 2% Mo and 0.1% N, exhibits the highest impedance value. Furthermore, Mo and N contents, temperature, and CO_2 gas influence the corrosion resistance of CA6NM. The increase in temperature without the addition of CO_2 gas in simulated geothermal brine decreases the corrosion resistance of CA6NM in simulated geothermal brine. By contrast, the increase in temperature accompanied by the addition of CO_2 gas increases the corrosion resistance of CA6NM in simulated geothermal brine.

6. Acknowledgments

All authors contributed equally to this work. All authors discussed the results and implications and commented on the manuscript at all stages. Gratitude is expressed to the Research Center for Metallurgy and Materials, Indonesian Institute of Sciences for financial support during this project in the fiscal year 2020.

7. References

[1] Hiroshi T, Li-Bin N, Hiromasa K, Naoki T, Kensuke M, Yoshihiro S, et al. Corrosion behavior of steam turbine materials for geothermal power plants. 14th International Conference on the Properties of Water and Steam; 2004 Aug 29 - Sep 3; Kyoto, Japan. Kyoto: IAPWS; 2004. p. 718-23.

[2] Mundhenk N, Huttenloch P, Babler R, Kohl T, Steger H, Zorn R. Electrochemical study of the corrosion of different alloys exposed to DE aerated 80°C geothermal brines containing CO_2. Corrosion Sci. 2014;84:180-8.

[3] Cabrini M, Lorenzi S, Pastore T, Favilla M, Perini R, Tarquini B. Materials selection for dew-point corrosion in geothermal fluids containing acid chloride. Geothermics. 2017;69:139-44.

[4] Carole L, Isadora NV, Thiago JM, Marc M, Ricardo PN, Gregory B, et al. Synergy between molybdenum and nitrogen on the pitting corrosion and passive film resistance of austenitic stainless steels as a pH-dependent effect. Mater Chem Phys. 2017;186:237-45.

[5] Mirakhorli F, Cao X, Pham XT, Wanjara P, Fihey JL. Phase structures and morphologies of tempered CA6NM stainless steel welded by hybrid laser-arc process. Mater Charact. 2017;123:264-74.

[6] Dawoud UM, Vanweele SF, Szklarska-Smialowska Z. The effect of H_2S on the crevice corrosion of AISI 410 and CA6NM stainless steels in 3.5% NaCl solutions. Corrosion Sci. 1992;32:295-306.

[7] Moch Syaiful A, Toni BR, Efendi M. Pitting resistance of the modified 13cr martensitic stainless steel in chloride solution. Int J Electrochem Sci. 2018;13:1515-26.

[8] Cesiulis H, Tsyntsaru N, Ramanavicius A, Ragoisha G. The study of thin films by electrochemical impedance spectroscopy. Nanostructures and thin films for multifunctional applications. New York: Springer; 2016. p. 3-42.

[9] Samaneh E, Mahmood A, Hossein S. Interpretation of cyclic potentiodynamic polarization test results for study corrosion behavior of metals : A Review. Protect Met Phys Chem Surface. 2018;54(5):976-89.

[10] Martin M, Virginie R, Rafael E, Marc M, Ricardo PN. Molybdenum effect on the sulfide stress corrosion of a super martensitic stainless steel in sour environment highlighted by electrochemical impedance spectroscopy. Electrochim Acta. 2017;252:58-66.

[11] Pfennig A, Wiegand R, Wolf M, Bork C. Corrosion and corrosion fatigue of AISI 420C (X46Cr13) at 60°C in CO2 -saturated artificial geothermal brine. Corrosion Sci. 2013;68:134-43.

[12] Jinlong L, Tongxiang L, Chen W. Surface enriched molybdenum enhancing the corrosion resistance of 316L stainless steel. Mater Lett. 2016;171:38-41.

[13] Brytan Z, Niagaj J, Reiman L. Corrosion studies using potentiodynamic and eis electrochemical techniques of welded lean duplex stainless steel UNS S82441. Appl Surf Sci. 2016;388:160-8.

[14] Mesquita TJ, Chauveau E, Mantel M, Kinsman N, Nogueira RP. Influence of Mo alloying on pitting corrosion of stainless steels used as concrete reinforcement. Rem Revista Escola de Minas. 2013;66:173-8.

[15] Tomio A, Sagara M, Doi T, Amaya H, Otsuka N, Kudo T. Role of alloyed molybdenum on corrosion resistance of austenitic Ni-Cr-Mo-Fe alloys in H_2S-Cl environments. Corrosion Sci. 2015;98:391-8.

[16] Moch Syaiful A, Bobby F, Arini N, Soesaptri O, Efendi M. Study of pitting resistance of rebar steels in jakarta coastal using simulated concrete pore solution. Proc Eng. 2017;171:517-25.

[17] Arini N, Muchlis AP, Rini R, Efendi M. Pitting corrosion resistance of CA6NM as geothermal turbine blade material in simulated artificial geothermal brine. IOP Conf Ser: Mater Sci Eng. 2019;541:012016.

[18] Niu L, Nakada K. Effect of chloride and sulfate ions in simulated boiler water on pitting corrosion behavior of 13Cr steel. Corrosion Sci. 2015;96:171-7.

[19] Mukhlis AP, Vinda P, Moch Syaiful A, Arini N, Efendi M. Mechanical properties of modified cast martensitic stainless steel CA6NM with addition of molybdenum and nitrogen. AIP Conf Proc. 2020;2232:060001.

[20] Efendi M, Moch Syaiful A, Siska P, Toni BR, Bintang A. Influence of Mo and Ni on microstructure and hardness of 13Cr martensitic stainless steel. Metalurgi. 2015;3:133-40.